Dark Channel Based Multiframe Super-Resolution Reconstruction

SHEN SHI [ID][1,2,3,4], **ZENGSHAN YIN** [ID][2,3], **ZHIMING MEI** [ID][2,3], **AND LONG WANG** [ID][2,3]

[1]Shanghai Institute of Microsystem and Information Technology, Chinese Academy of Sciences, Shanghai 200050, China
[2]Innovation Academy for Microsatellites, Chinese Academy of Sciences, Shanghai 201210, China
[3]University of Chinese Academy of Sciences, Beijing 100049, China
[4]School of Information Science and Technology, ShanghaiTech University, Shanghai 201210, China

Corresponding author: Shen Shi (shishen@shanghaitech.edu.cn)

ABSTRACT Multiframe super-resolution (MFSR) can obtain a high-resolution image from a set of low-resolution images. The performance of super-resolution is affected by the image prior information. The current super-resolution algorithms typically use total variation prior and its improved version, restoring the image edges well. However, it will produce artifacts and stair effects in the smooth region of the image. Therefore, we propose a dark channel-based MFSR algorithm to achieve edge-preserving and noise-suppressing. Firstly, the total variation prior is used to ensure the edge-preserving ability of the algorithm. Secondly, the dark channel prior is added to suppress artifacts and stair effects. Finally, the weights of the prior terms are iteratively adapted to obtain the final high-resolution image. Experiments show that the proposed algorithm can achieve a better result in objective and subjective visual evaluations.

INDEX TERMS Image process, multiframe super-resolution, dark channel prior, total variation prior, image prior combination, Bayesian framework.

I. INTRODUCTION

Resolution is a basic feature of an image, and it is also the major factor limiting the scope of image application [1], [2]. Increasing the resolution of images can effectively expand the scope of image applications. Super-resolution (SR) can improve the resolution of images via mathematical methods without changing the hardware of imaging system [3]. This technology has great advantages in cost and it is widely used in remote sensing, medical imaging, and other fields [4]–[7].

The SR methods have been developed for decades. In 1984, Tsai and Huang proposed a frequency domain based multiframe super-resolution (MFSR) algorithm [8], which proved the theoretical feasibility of image SR. The algorithm reconstructed the high-resolution (HR) image by the existing sub-pixel displacement between the low-resolution (LR) images, and was successfully applied to the LANDSAT images. Kim *et al.* [9] improved the MFSR algorithm by analyzing the noise and blur characteristics of the images. Bose *et al.* [10] further optimized the MFSR algorithm by

The associate editor coordinating the review of this manuscript and approving it for publication was Sudhakar Radhakrishnan [ID].

analyzing the registration error in the reconstruction process, which expanded the application range of the algorithm. Rhee and Kang [11] used discrete cosine transform (DCT) instead of discrete Fourier transform (DFT) in the MFSR algorithm, which can effectively improve the computational efficiency of the algorithm. Because the MFSR algorithm based on the frequency domain was simple in principle, fast in calculation speed, and low in computing hardware requirements, it can be easily implemented in engineering. However, in this type of algorithms, only the global transformation motion could be handled, and the prior information could not be used.

In order to solve the aforementioned problems, a series of MFSR algorithms have been proposed. These algorithms use the sub-pixel shifts between multiple LR images to provide additional information for reconstructing HR images, including nonlinear interpolation method [12]–[14], iterative back projection (IBP) [14]–[17], projection onto convex sets (POCS) [18]–[20], maximum likelihood (ML) estimation [21], [22], maximum a posteriori probability (MAP) [23]–[27], adaptive filtering [28], [29] and other methods. The image MFSR problem is an ill-posed problem. By adding image prior information, the ill-posed inverse

problem is constrained as a well-posed problem, so that the reconstruction result converges to obtain a stable solution. Generally, the reconstruction results of the spatial domain algorithm are better than the frequency domain algorithm, but the spatial domain algorithm is sensitive to image prior knowledge and registration information.

The image prior information has a decisive effect on MFSR, and different prior information will lead to different reconstruction results. The earliest image prior is the Laplace prior [30], [31]. In this prior, the natural images are assumed to be smooth, and noise will lead to image smoothness characteristic loss. By imposing penalty constraints on the high-frequency components of the reconstructed image, the noise can be limited, and a smooth solution can be obtained. However, it will result in blurred edges and loss of texture information. In the Gaussian Markov Random Field (GMRF) prior [32], by analyzing the distribution of each image pixel and its neighboring pixels information, the details and texture can be distinguished. In the Huber Markov Random Field (HMRF) prior [33], the image is assumed to be block smoothed. Compared with GMRF prior, the HMRF prior uses the Huber function, instead of the smoothness measurement function, to measure the image spatial characteristics. Then, the details in the edges can be preserved, and the noise in the smooth regions can be suppressed.

The total variation prior (TV) [34]–[38] is widely used in image deblurring, image denoising, and image MFSR. However, this prior will produce stair effects in the smooth area of images under strong noise. Farsiu *et al.* [30] proposed a bilateral total variation (BTV) prior. In the BTV prior, by comparing the original image with the translated image, a larger weighted coefficient was assigned to the edge areas, and a smaller weighted coefficient was assigned to the smooth areas. Then a more robust result with more details can be achieved.

Since different image priors have different effects on image reconstruction, combining image priors became an effective way to improve the quality of reconstructed images. Chantas *et al.* [39] combined the TV prior and the Product of Expert (PoE) prior [40] to a new image prior, which was able to simultaneously enforce the properties on the image. Villena *et al.* [41] applied a combination of the sparse TV prior and l_1 prior, and the non-sparse simultaneous auto-regressive (SAR) prior to the MFSR. This prior could integrate the strong edge preservation of the sparse prior and the smoothness of the non-sparse prior. In [42], a spatially adaptive linear filter prior was proposed for the MFSR. In [43], a filter bank and l_1 norm based prior combination method was presented. However, these methods still produce artifacts and stair effects because the combined priors were both based on the gradient properties of the image.

The dark channel is introduced by He *et al.* [44] for single image dehazing, then Pan *et al.* [45] modify the prior that the dark channel of natural images is sparse instead of zero and enforce the sparsity for kernel estimation. Inspired by the

work in [45]–[47], we note that the DC pixels are less sparse after the degradation process. Therefore, we introduce the DC prior into MFSR algorithm.

In order to overcome the aforementioned shortcomings, in this paper, we proposed a new algorithm to improve the quality of the reconstructed image, and the main contributions are as follows:

1) Introduce the dark channel (DC) prior to super-resolution, in order to suppress the artifact and stair effects during the image edges recovering.
2) Propose a new MFSR algorithm by combining the DC and TV prior, which can effectively improve the MFSR effect.
3) Experiment results verify that the above algorithm can achieve better performance in both PSNR and SSIM.

The rest of this paper is organized as follows. In Section II, we build the entire super resolution model. In Section III, we give the detailed description of the DC-TV based MFSR algorithm. Then, in Section IV, we represent the experiment results and evaluate the proposed algorithm in comparison with other representative benchmarks. Finally, we concluded this paper in Section V.

II. THE SUPER-RESOLUTION RECONSTRUCTION MODEL

The super-resolution reconstruction model is composed of image observation model, image noise model, image prior model, and image registration model.

A. OBSERVATION MODEL

The observation model is established to describe the relationship between HR images and LR images. An LR image with $N = N_1 \times N_2$ pixels (where N_1 and N_2 are the row number and column number of the image)can be obtained from an HR image with $P^2N = PN_1 \times PN_2$ pixels(P is the up-sampling factor) through a series of operations such as rotation, displacement, blurring, down-sampling, and mixed noise. The corresponding observation model is represented by the Fig. 1.
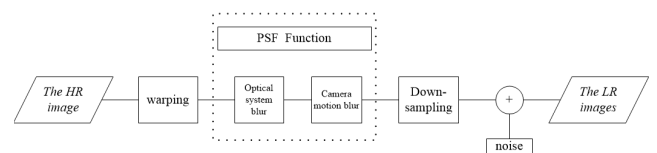

FIGURE 1. Observation model relating LR images to the HR image.

According to this observation model, a mathematical model can be established in matrix-vector form

$$I_l^L = SK_l W_{M_l} I^H + n_l, l = 1, 2, \ldots, s, \tag{1}$$

where s is the number of the LR images, $I^H \in R^{P^2N \times 1}$ and $I_l^L \in R^N \times 1$ are lexicographically ordered vectors used to represent HR and LR images respectively. W_{M_l} is the motion transformation matrix with size $P^2N \times P^2N$, and

the value is affected by the motion transformation parameters $M_l = \{\theta_l, d_{hl}, d_{vl}\}$. K_l is the blurring matrix with size $P^2N \times P^2N$, and S is the down-sampling matrix with size $N \times P^2N$. n_l represents the additive noise vector related to the lth LR image.

B. IMAGE NOISE MODEL

The noise model of the image corresponds to the degradation relationship between the LR images and the HR image. The relationship can be expressed as the conditional probability density function $p(I_l^L \mid I^H)$ of the LR image. Assuming that the noise is additive white Gaussian noise (AWGN) with the variance η_l^{-1}, according to (1), the noise model of the image can be expressed as

$$p(I_l^L \mid I^H, M_l, \eta_l) \propto \eta_l^{\frac{N}{2}} \, exp\left\{-\frac{\eta_l}{2}\left\|I_l^L - SKW_{M_l}I^H\right\|_2^2\right\},$$

(2)

Since the LR images are captured independently, the noises can be assumed to be statistical independence. Therefore, we can obtain the following expression

$$p(I^L \mid I^H, \mathcal{M}, \{\eta_l\}) = \prod_{l=1}^{s} p(I_l^L \mid I^H, M_l, \eta_l),$$

(3)

where the $I^L = \{I_1^L, I_2^L, \dots, I_s^L\}$ is the set of LR images and $\mathcal{M} = \{M_1, M_2, \dots, M_s\}$ is the set of registration parameters.

C. IMAGE PRIOR MODEL

Two image prior model is used in this paper, the TV prior model $p(I^H \mid \eta_{tv})$ controlled by hyperparameter η_{tv} and the DC prior model $p(I^H \mid \eta_d)$ controlled by hyperparameter η_d.

1) TV PRIOR MODEL

The TV prior is widely used because of the property of edge preserving [48]. The mathematical expression of the image TV prior is

$$p(I^H \mid \eta_{tv}) \propto \eta_{tv}^{\frac{P^2N}{2}} \, exp\left\{-\frac{\eta_{tv}}{2}TV(I^H)\right\},$$

(4)

where $TV(I^H)$ has two different expressions, i.e.

$$TV(I^H) = \sum_i \sqrt{(\Delta_{hi}(I^H))^2 + (\Delta_{vi}(I^H))^2}$$

(5)

and

$$TV(I^H) = \sum_i |\Delta_{hi}(I^H)| + |\Delta_{vi}(I^H)|.$$

(6)

In (5) and (6), $\Delta_{hi}(I) = I(i) - I(r(i))$ and $\Delta_{vi}(I) = I(i) - I(b(i))$ respectively represents the horizontal and vertical gradient of the image. Equation (5) is called the isotropic TV model and (6) is called the anisotropic TV model. We use the isotropic TV model in this paper, because compared to the anisotropic TV model, the isotropic TV model is more robust to image rotation, image reflection, and image position transformation, and the reconstruction effect of the isotropic TV model is also better than the anisotropic TV model [49].

2) DC PRIOR MODEL

The mathematical expression of the image DC prior model is

$$p(I^H \mid \eta_d) \propto \eta_d^{\frac{P^2N}{2}} \, exp\left\{-\frac{\eta_d}{2}\left\|D(I^H)\right\|_0\right\},$$

(7)

where the $D(I^H)$ represents the DC of the image.

The standard form of DC is expressed by

$$D(I_i) = \min_{j \in \mathcal{N}(i)} I_j,$$

(8)

where i and j are image pixel indexes and $\mathcal{N}(i)$ is an image patch centered at i. Note that the nonlinear operation $D(I_i)$ cannot be directly used in the subsequent solution. Hence, a linear operation D_c which is equivalent to this nonlinear operation is applied in the following form

$$D(I_i) = \min_{j \in \mathcal{N}(i)} I_j = D_c(i, :)I.$$

(9)

The D_c in (9) is a matrix with size $P^2N \times P^2N$ and the elements in ith row is acquired from the below formula

$$D_c(i, j) = \begin{cases} 1 & j = q \\ 0 & otherwise, \end{cases}$$

(10)

where q is the position index of the minimum value in the given neighborhood $\mathcal{N}(i)$.

D. IMAGE REGISTRATION MODEL

The registration model aims to describe the motion transformation relation between the target images and the reference image. The registration parameters are generally obtained by using the first frame of the LR images as reference. In contrast, we use the HR image as reference to obtain more accurate registration parameters.

Using a 3-parameters motion model, the position relationship between the reference image and the lth warped image is

$$\begin{pmatrix} x_l \\ y_l \end{pmatrix} = \begin{pmatrix} cos\theta_l & -sin\theta_l \\ sin\theta_l & cos\theta_l \end{pmatrix}\begin{pmatrix} x \\ y \end{pmatrix} + \begin{pmatrix} d_{hl} \\ d_{vl} \end{pmatrix},$$

(11)

where (x, y) are the coordinates of the reference image and (x_l, y_l) are the coordinates of the warped image. $M_l = (\theta_l, d_{hl}, d_{vl})$ respectively correspond to the rotation angle, horizontal displacement, and vertical displacement in the motion transformation.

Since the coordinates (x_l, y_l) are generally not integer values, the grid of the lth warped image should be calculated by resampling (see Fig. 2). By using the bilinear interpolation method to approximate the lth warped image, the value of the pixels can be calculated by the weighted sum of four adjacent points, that is

$$W_{M_l}I^H \approx D_{a_x}D_{a_y}I_{se} + (E - D_{a_x})(E - D_{a_y})I_{nw}$$
$$+ (E - D_{a_x})D_{a_y}I_{sw} + D_{a_x}(E - D_{a_y})I_{ne},$$

(12)

where $I_{se}, I_{ne}, I_{sw}, I_{nw}$ respectively represent four adjacent points in different directions around the target point. E is the identity matrix, D_{a_x} and D_{a_y} are diagonal matrices with a_x, a_y as diagonal elements. $[a_x, a_y]^T$ represent the distance

between the pixel point and the point located at the northwest. The values of $[a_x, a_y]^T$ can be calculated by the following formula

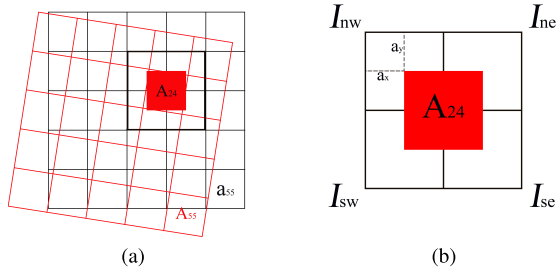$$\begin{cases} a_x = x_l - floor(x_l) \\ a_y = y_l - floor(y_l). \end{cases} \quad (13)$$

FIGURE 2. The resampling process of the image registration model. (a) The reference image grid (in black) and the *l*th warped image grid (in red). (b) Detailed view of (a), with the pixels used for the re-sampled grid element A_{24}.

III. DC-TV BASED MFSR ALGORITHM

The MFSR is an inverse processing of the image degradation. The MFSR equation is an ill-posed problem and cannot be directly solved. Therefore, the Bayesian Maximum a Posteriori (MAP) estimation method is used. Then the MFSR aims to find an estimate of I^H which can maximize the probability density function $p(I^H \mid I^L)$, i.e.

$$\{\hat{I}^H, \hat{\mathcal{M}}, \hat{\Theta}\} = \arg\max_{I^H, \mathcal{M}, \Theta} p\left(I^H, \mathcal{M}, \Theta \mid I^L\right). \quad (14)$$

where $\Theta = \{\{\eta_1, \eta_2, \ldots, \eta_s\}, \eta_{tv}, \eta_d\}$ is the set of hyperparameters. Using the Bayesian inference rule, we have

$$p(I^H, \mathcal{M}, \Theta \mid I^L) = \frac{p(I^H, \mathcal{M}, \Theta, I^L)}{p(I^L)}, \quad (15)$$

where the conditional distribution can be expressed as

$$p(I^H, \mathcal{M}, \Theta, I^L) = p(I^L | I^H, \mathcal{M}, \{\eta_l\}) p(I^H \mid \eta_{tv}, \eta_d) \\ \cdot \prod_{l=1}^{s} p(M_l) \prod_{l=1}^{s} p(\eta_l) p(\eta_{tv}) p(\eta_d). \quad (16)$$

The mathematical derivation is given in this section, and the flowchart is shown in Fig. 3. Since the main contribution of the proposed algorithm is the combination of the DC and TV prior, we will first describe the image prior optimization steps as follows.

A. THE PRIOR OPTIMIZATION

A combined prior named DC-TV is proposed to improve the effect of the MFSR algorithm. The TV prior could preserve the image edges by distinguishing between gradient change areas and image smooth areas, but cannot get rid of the noise. In addition, the DC prior have the ability to suppress the noise by the sparse property of the l_0 norm. Thus, the DC-TV prior can effectively combined the edge preserving capability of
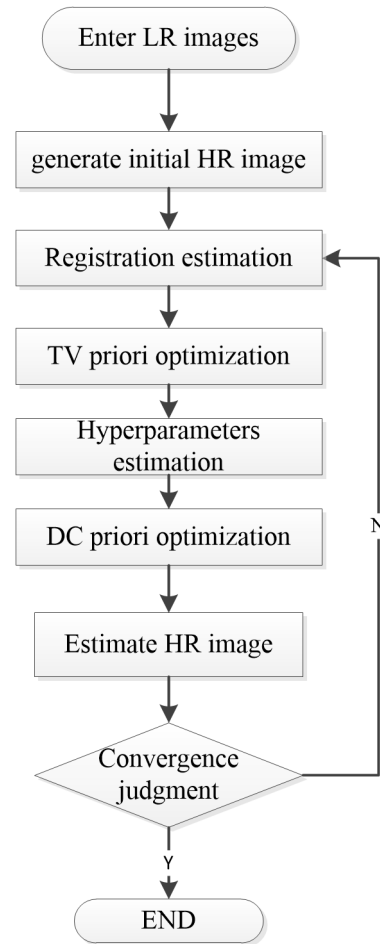

FIGURE 3. The flowchart of the proposed algorithm.

the TV prior and noise suppressing capability of the DC prior. The expression of the DC-TV prior model is,

$$p(I^H \mid \eta_{tv}, \eta_d) = p(I^H \mid \eta_{tv}) p(I^H | \eta_d). \quad (17)$$

where $p(I^H \mid \eta_{tv})$ and $p(I^H | \eta_d)$ represent the TV prior and the DC prior, respectively.

1) TV PRIOR OPTIMIZATION

The TV prior equation (5) cannot be directly tackled in the proposed algorithm, so the majorization-minimization (MM) approach [50] are used. Considering the follow inequality

$$\sqrt{z} \le \frac{z + u}{2\sqrt{u}}, \quad (18)$$

where $u > 0, z > 0$, and the equation is established when $u = z$.

For the ith pixel of the image, we introduce a variable

$$Q_{tv}(I_i^H, u_i) = \frac{(\Delta_{hi}(I^H))^2 + (\Delta_{vi}(I^H))^2 + u_i^2}{2u_i}. \quad (19)$$

Thereby, $Q_{tv}(I_i^H, u_i)$ has a minimum value equal to $\|\nabla I^H\|$, i.e.

$$Q_{tv}(I_i^H, u_i) \ge \left\|\nabla I^H\right\| = \sqrt{(\Delta_{hi}(I^H))^2 + (\Delta_{vi}(I^H))^2}. \quad (20)$$

Hence, the TV prior model can be approximated as

$$p(I^H \mid \eta_{tv}) \propto \eta_{tv}^{\frac{P^2 N}{2}} exp\left\{-\frac{\eta_{tv}}{2} Q_{tv}(I^H, U)\right\}. \quad (21)$$

where the U is a diagonal matrix of size $P^2 N \times P^2 N$ with diagonal elements calculated

$$U_{ii} = \sqrt{(\Delta_{hi}(I^H))^2 + (\Delta_{vi}(I^H))^2 + \varepsilon^2}. \quad (22)$$

2) DC PRIOR OPTIMIZATION

In the DC prior equation, the half-quadratic splitting L_0 minimization approach [51] is proposed to tackle the L_0 norm. By introducing an auxiliary vector g, $\|D(I^H)\|_0$ can be approximated in the following form

$$Q_D(I^H, g) = \eta_g \left\|D_c I^H - g\right\|_2^2 + \|g\|_0, \quad (23)$$

where η_g is a penalty parameter. When η_g tends to infinity, $\|D(I^H)\|_0$ and $Q_D(I^H, g)$ are approximately equal. Calculate the auxiliary vector g by minimizing (23), that is

$$\hat{g} = \arg\min_{g} \eta_g \left\|D_c I^H - g\right\|_2^2 + \|g\|_0. \quad (24)$$

Thus, the solution of g is

$$\hat{g} = \begin{cases} D_c I^H & (D_c I^H) \geq \frac{1}{\eta_g} \\ 0 & otherwise. \end{cases} \quad (25)$$

This optimization updates g and D_c iteratively by amplifying η_g so that $Q_D(I^H, g)$ approximately equal to $\|D(I^H)\|_0$. Hence, The DC prior model can be approximated as

$$p(I^H \mid \eta_d) \propto \eta_d^{\frac{P^2 N}{2}} exp\left\{-\frac{\eta_d}{2} Q_D(I^H, g)\right\}. \quad (26)$$

B. REGISTRATION ESTIMATION

The sub-pixel registration is an important part of MFSR. It is mainly obtained by interpolating between pixels. The denser these pixels of the HR image are, the more realistic the interpolation effect is, and the more accurate the registration result becomes. Assuming that the registration parameters obeys the multivariate Gaussian distribution [52], i.e.,

$$p(M_l) = \mathcal{N}(M_l|\bar{M}_l, \zeta_l), \quad (27)$$

where $\bar{M}_l$ is the preliminary registration parameters and ζ_l is a priori covariance matrix.

After the MFSR image estimation I^H is obtained, the parameter M_l can be estimated by minimizing the following equation

$$\hat{M}_l = \arg\max_{M_l} p(I_l^L|I^H, M_l, \eta_l)p(M_l) \quad (28)$$

which can be simplified by a logarithmic form, i.e.,

$$\hat{M}_l = \arg\min_{M_l} \eta_l \left\|I_l^L - SKW_{M_l}I^H\right\|_2^2 \\ + (M_l - \bar{M}_l)^T(\zeta_l^n)^{-1}(M_l - \bar{M}_l). \quad (29)$$

Since $W_{M_l}I^H$ is nonlinear with respect to M_l, we perform a first-order Taylor expansion on $W_{M_l}I^H$ at the value $\bar{M}_l$, i.e.

$$W_{M_l}I^H = W_{\bar{M}_l}I^H + J_{\bar{M}_l}(M_l - \bar{M}_l), \quad (30)$$

where $J_{\bar{M}_l}$ is the Jacobian matrix and it can be calculated by

$$J_{M_l} = \frac{\partial(W_{M_l}I^H)}{\partial M_l}$$
$$= \frac{\partial(W_{M_l}I^H)}{\partial\left(\left[a_x^T, a_y^T\right]^T\right)} \frac{\partial\left(\left[a_x^T, a_y^T\right]^T\right)}{\partial\left(\left[x_l^T, y_l^T\right]^T\right)} \frac{\partial\left(\left[x_l^T, y_l^T\right]^T\right)}{\partial M_l}. \quad (31)$$

The three parts of (31) can be calculated by (11), (12) and (13), respectively. Hence, the final value [53] of $J_{\bar{M}_l}$ is in the form

$$J_{M_l} = \left[P_{1M_l}B_{1M_l} + P_{2M_l}B_{2M_l}, B_{1M_l}, B_{2M_l}\right], \quad (32)$$

where we have

$$P_{1M_l} = diag(-xsin(\theta_l) - ycos(\theta_l)), \quad (33)$$
$$P_{2M_l} = diag(xcos(\theta_l) - ysin(\theta_l)), \quad (34)$$
$$B_{1M_l} = (E - D_{a_y})(I_{ne} - I_{nw}) + D_{a_y}(I_{se} - I_{sw}), \quad (35)$$

and

$$B_{1M_l} = (E - D_{a_x})(I_{sw} - I_{nw}) + D_{a_x}(I_{se} - I_{ne}). \quad (36)$$

Substituting (32) into (29), the registration parameters M_l can be solved by

$$(\zeta_l^{n+1})^{-1}M_l = (\zeta_l^n)^{-1}\bar{M}_l + \eta_l(SKJ_{\bar{M}_l})^T SKJ_{\bar{M}_l} \\ + \eta_l(SKJ_{\bar{M}_l})^T(I_l^L - SKW_{\bar{M}_l}I^H) \quad (37)$$

with

$$(\zeta_l^{n+1})^{-1} = (\zeta_l^n)^{-1} + \eta_l(SKJ_{M_l})^T SKJ_{M_l}, \quad (38)$$

where n is the number of iterations and the initial $\zeta_l = \eta_l(SKJ_{\bar{M}_l})^T SKJ_{\bar{M}_l}$ is calculated by the initial registration parameters $\bar{M}_l$.

C. ESTIMATION OF THE HYPERPARAMETERS

Generally, the distributions of hyperparameters $\{\eta_l\}$ and η_{tv} are Gamma distributions [54], i.e.

$$p(w) = \Gamma(w|a_w, b_w) = \frac{(b_w)^{a_w}}{\Gamma(a_w)} w^{a_w - 1} exp\{-b_w w\}, \quad (39)$$

where w denotes the hyperparameter. Meanwhile, $a_w > 0$ and $b_w > 0$ are the shape and scale parameters of the Gamma distributions, respectively. In our experiments, these parameters are settled with $a_w = 1$ and $b_w = 0.1$.

Therefore, the hyperparameters $\{\eta_l\}$ can be calculated by the following equation

$$\hat{\eta}_l = \arg\max_{\eta_l} p(I_l^L|I^H, M_l, \eta_l)p(\eta_l). \quad (40)$$

Substituting (2) and (39) into (40), the estimate of η_l is

$$\hat{\eta}_l = \frac{N + 2a_{\eta_l} - 2}{2b_{\eta_l} + \left\| I_l^L - SKW_{M_l}I^H \right\|_2^2}. \tag{41}$$

The hyperparameter η_{tv} can be calculated in the following equation,

$$\hat{\eta}_{tv} = \arg\max_{\eta_{tv}} p(I^H|\eta_{tv})p(\eta_{tv}). \tag{42}$$

Substituting (4) and (39) into (42), the estimate of η_{tv} is

$$\hat{\eta}_{tv} = \frac{P^2N + 2a_{\eta_{tv}} - 2}{2b_{\eta_{tv}} + \sum_{i=1}^{P^2N} \sqrt{(\Delta_{hi}(I^H))^2 + (\Delta_{vi}(I^H))^2}}. \tag{43}$$

The η_d is an empirical hyperparameter, and its value in our experiments is

$$\eta_d = 0.1 \times \eta_{tv}. \tag{44}$$

D. ESTIMATION OF HR IMAGE

After obtaining the image registration parameters $\mathcal{M}$, and the hyperparameters Θ, the HR image I^H can be estimated by the following equation

$$\hat{I}^H = \arg\max_{I^H} p(I^L|I^H, \mathcal{M}, \{\eta_l\})p(I^H) \tag{45}$$

Substituting the optimization expression (19) and (23) into (17), the MFSR solution formula can be simplified in the form

$$\left[\Sigma_{I^H}\right]^{-1}I^H = \sum_{l}^{s} \eta_l\left[SKW_{M_l}\right]^T I_l^L + \eta_d\eta_g D_c^T g, \tag{46}$$

where

$$\left[\Sigma_{I^H}\right]^{-1} = \sum_{l=1}^{s} \eta_l[SKW_{M_l}]^T SKW_{M_l}$$
$$+ \eta_{tv}(\Delta_h^T U^{-1}\Delta_h + \Delta_v^T U^{-1}\Delta_v) + \eta_d\eta_g(D_c^T D_c). \tag{47}$$

The reconstruction process of the proposed algorithm includes the registration parameters estimation, the prior term optimization, the hyperparameters estimation, and the high-resolution image estimation. The stable solution of the algorithm can be obtained by looping the reconstruction process, and the loop termination condition is

$$\frac{\left\| I^{H^t} - I^{H^{t-1}} \right\|_2^2}{\left\| I^{H^t} \right\|_2^2} \leq \varepsilon_1. \tag{48}$$

where t is the iteration counter, and I^{H^0} is a zero vector. The pseudo code of the algorithm is given in Algorithm 1.

In Algorithm 1, the first loop describing the reconstruction process of the algorithm, and the second loop describing the DC prior optimization. η_g is the parameter used during the DC prior optimization process, and the value of η_g is between $\eta_g^{init} = 0.001$ and $\eta_g^{max} = 8$.

Algorithm 1 MFSR Using DC-TV Prior

Input: LR images I^L, up-sampling factor P, iteration counter $t = 1$.
Output: HR image I^{H^t}.
1: Estimate I^{H^1} by bicubic methods.
2: **while** termination condition (48) is not met **do**
3:　　Estimate M_l by I^{H^t} and (37).
4:　　Estimate U by I^{H^t} and (22).
5:　　Estimate $\eta_l, \eta_{tv}, \eta_d$ by I^{H^t}, (41), (43), and (44).
6:　　$\hat{I}^H = I^{H^t}$.
7:　　$\eta_g = \eta_g^{init}$.
8:　　**while** $\eta_g < \eta_g^{max}$ **do**
9:　　　　Estimate D_c by $\hat{I}^H$ and (10).
10:　　　Estimate g by $\hat{I}^H$ and (25).
11:　　　Update $\hat{I}^H$ by (46).
12:　　　$\eta_g = \eta_g \times 2$.
13:　　**end while**
14:　　$t = t + 1$.
15:　　$I^{H^t} = \hat{I}^H$.
16: **end while**

IV. EXPERIMENTAL RESULTS

In the proposed DC-TV based MFSR algorithm, the TV prior and DC prior were combined to simultaneously enhance the edge preservation and stair effects suppression capability. To evaluate the performance of the proposed algorithm, multiple sets of simulated images and real data are used in the experiment. The experimental results on simulated images can be evaluated by using objective evaluation criteria, such as Peak Signal to Noise Ratio (PSNR) and Structural Similarity (SSIM). The experimental results on real data can intuitively reveal the advantages of the proposed algorithm.

A. EXPERIMENTS WITH SIMULATED IMAGE

Four images (Fig. 4) are employed in the simulation experiments. Each original image is utilized to create 5 synthetic images by image degradation model according to (1). The degradation process includes the following steps.

- Warp images with rotation and translation. The rotation angles are

$$\left(0°, 3°, -3°, 5°, -5°\right), \tag{49}$$

and the translations are

$$\begin{pmatrix} 0 \\ 0 \end{pmatrix}, \begin{pmatrix} 0 \\ 0.5 \end{pmatrix}, \begin{pmatrix} 0.5 \\ 0 \end{pmatrix}, \begin{pmatrix} 1 \\ 0 \end{pmatrix}, \begin{pmatrix} 0 \\ 1 \end{pmatrix}, \tag{50}$$

pixels, respectively.
- Blur images by 3×3 Gaussian PSF with standard deviation 1.
- Down-sample images with a factor of 2.
- Add independent identically distributed Gaussian noise. Five different SNR levels (5dB, 15dB, 25dB, 35dB and 45dB) are selected for our experiments.

For the evaluation of our proposed algorithm, we compare it with 1) bicubic interpolation, 2) the variational MFSR
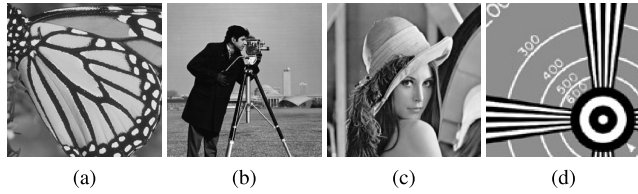
FIGURE 4. Four images that often used in MFSR experiments. (a) butterfly, (b) cameraman, (c) lena, (d) EIAcen.

method with SAR prior, 3) the variational MFSR method with TV prior, 4) the nonstationary prior combination method [42] with the filter combination NF3, and 5) the l_1 norm based prior combination method [43] with the filter combination NF2. The bicubic interpolation algorithm is simple and easy to implement, but the results are relatively poor. The MFSR method with SAR prior has robust noise suppression effects, while the MFSR method with TV prior have strong edge preservation capabilities. The combined prior NF3 and combined prior NF2 are the best selection in the MFSR method [42] and the MFSR method [43], respectively, which are denoted as NS_NF3 and NL1_NF2 to make a distinction.

When quantifying the gain of these priors, the PSNR and SSIM are exploited as our indicators. With different prior information and SNR levels, the PSNR of four reconstructed images are shown in Fig. 5, and the SSIM of four reconstructed images are shown in Fig. 6. Both of them are obtained by all the MFSR algorithms we need to compare with.
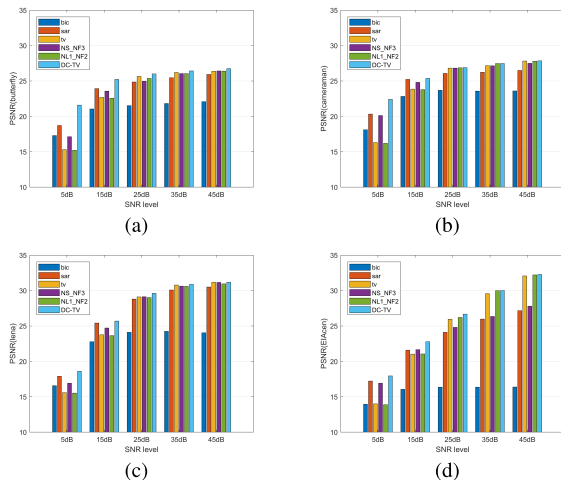
FIGURE 5. Comparison of PSNR of MFSR algorithms with different image priors for different images. (a) butterfly, (b) cameraman, (c) lena, (d) EIAcen.

As shown in Fig. 5, the proposed DC-TV prior outperforms other comparative methods at five different SNR levels. And in Fig. 6, it can be observed that the proposed DC-TV prior creates distinct advantages on both noise suppression and edge structure preservation.

To demonstrate the performance in the case of low SNR, the experiment results of 5dB image SNR is shown in Fig. 7.
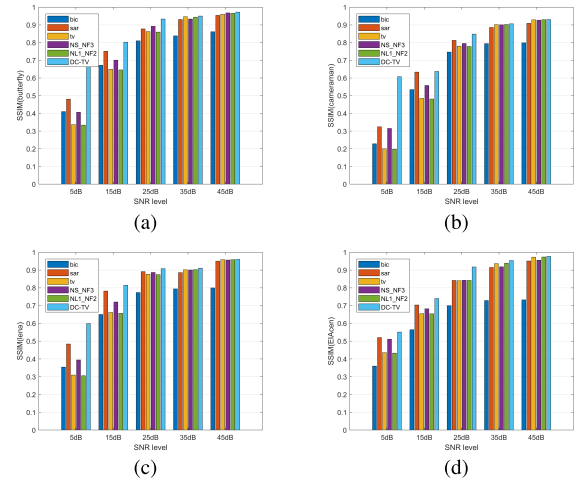

FIGURE 6. Comparison of SSIM of MFSR algorithms with different image priors. (a) butterfly, (b) cameraman, (c) lena, (d) EIAcen.

Obviously, both the SAR and NS_NF3 prior algorithm performed better than the bicubic interpolation in Fig. 7, while the TV and NL1_NF2 prior algorithm are inferior to the bicubic interpolation. Specially, our proposed DC-TV prior algorithm significantly outperformed the others. It indicates that the SAR and NS_NF3 prior algorithm can effectively suppress noise and reconstruct images when noise becomes the main factor in image quality degradation.
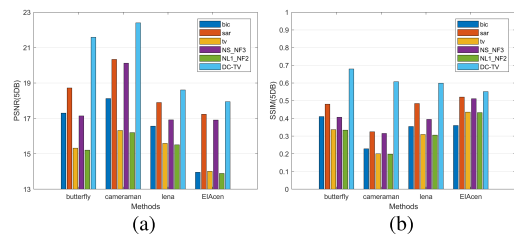

FIGURE 7. Comparison of MFSR algorithms with different image priors when the SNR is 5dB. (a) PSNR, (b) SSIM.

When the image SNR is 25dB, as shown in Fig. 8, the SAR, TV, NS_NF3, and NL1_NF2 prior algorithms achieved similar reconstruction effects, all of which are worse than the bilinear interpolation. In Fig. 8, the PSNR of SAR and NS_NF3 is worse than TV and NL1_NF2, while the SSIM of SAR and NS_NF3 is better than that of TV and NL1_NF2. Moreover, the performance of DC-TV prior algorithm obviously surpassed other algorithms.

When the image SNR is 45dB, as shown in Fig. 9, noise has less influence on the image quality. In this situation, most of the listed algorithms have achieved relatively good image reconstruction results, except for the bilinear interpolation. The performance of the DC-TV algorithm is still better than other comparative algorithms. It proved that the DC-TV algorithm could suppress noise without compromising the edge preserving capability of the TV prior.
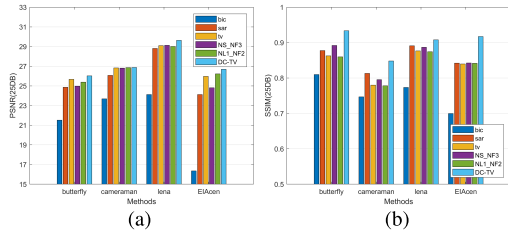
FIGURE 8. Comparison of MFSR algorithms with different image priors when the SNR is 25dB. (a) PSNR, (b) SSIM.
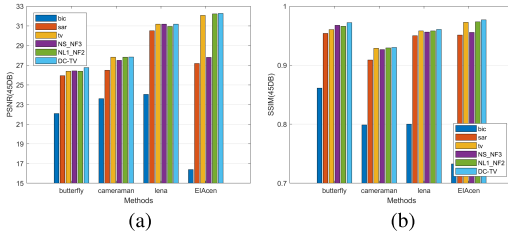

FIGURE 9. Comparison of MFSR algorithms with different image priors when the SNR is 45dB. (a) PSNR, (b) SSIM.

B. EXPERIMENTS WITH REAL DATA

In addition to the aforementioned simulation experiments, two sets of real image sequences have been used to verify our proposed algorithm. These two sets were collected from http://www.soe.ucsc.edu/ milanfar/software/sr-datasets.html and are representative, widely used for experiments in many papers on the MFSR algorithms.

The first set contains 35 frames of real images about *word*, and the second set contains 20 ones about *disk*. Both of them approximately follow the global translational motion model. In our experiment, these two image sets were reconstructed with a magnification of 2, with the results shown in Fig. 10 and Fig. 11.

Since there are no original HR images corresponding to the real LR images, objective indicators such as PSNR and SSIM cannot be used for experimental evaluation anymore. Thus, subjective observation is employed to evaluate the reconstruction effect based on real data.

For the *word* image sequence in Fig. 10, the result of bicubic interpolation algorithm is too blurry to recognize. The image edges of the SAR prior are smooth but blurred. And that of the TV prior is seriously affected by the stair effects. In contract, the NS_NF3 algorithm can effectively suppress the stair effects in the smoothing area of the image, and the NL1_NF2 algorithm has clear edges with less stair effects. Moreover, the reconstructed image of our proposed algorithm has the best visual performance with clear edges and no stair effects.

Similarly, for the *disk* image sequence in Fig. 11, the reconstructed image of bicubic interpolation algorithm is still blurred, and the SAR prior is affected by artifacts. The results of both the TV and NL1_NF2 prior are affected by the stair effects. As a contrast, the NS_NF3 algorithm has the best noise suppression effect, but over-smooths the image which leads to the loss of edge information. As expected, the result
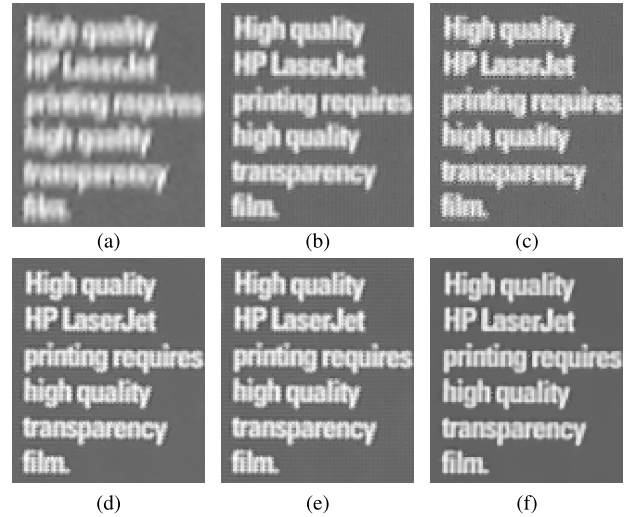

FIGURE 10. Comparison of reconstruction results based on an image sequence about *word*. (a) the result of bicubic interpolation algorithm; (b) the result of SAR prior; (c) the result of TV prior; (d) the result of NS_NF3 prior; (e) the result of NL1_NF2 prior; (f) the result of our proposed DC-TV prior algorithm.
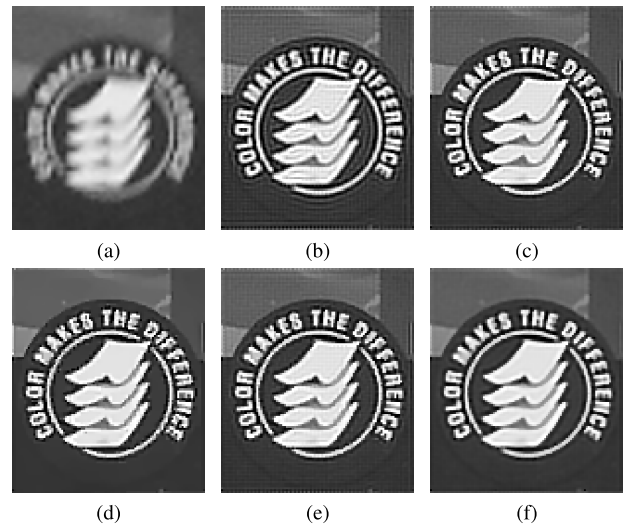

FIGURE 11. Comparison of reconstruction results based on an image sequence about *disk*. (a) the result of bicubic interpolation algorithm; (b) the result of SAR prior; (c) the result of TV prior; (d) the result of NS_NF3 prior; (e) the result of NL1_NF2 prior; (f) the result of the proposed algorithm with DC-TV prior.

of our proposed algorithm has clear image edges, with less influence of artifacts and stair effects, and the visual effect is significantly better than other comparative algorithms.

V. CONCLUSION

In this paper, we introduced the DC prior to super-resolution. By analyzing the sparse characteristics of the image DC prior, this can be utilized to suppress the artifact and stair effects during the edges recovering. Based on this superiority, we proposed an MFSR algorithm by combining the DC and TV prior. The experiments with simulated and real images verified the effectiveness and robustness of our proposed algorithm. For different SNR levels, our algorithm have higher PSNR and SSIM values, especially in the case of low

SNR. For real images, our proposed algorithm have the better visual effect. In the future work, we will optimize the algorithm to reduce its computational complexity, so that the DC prior can be extended to the hyperspectral image processing for better noise suppression.

REFERENCES

[1] S. C. Park, M. K. Park, and M. G. Kang, "Super-resolution image reconstruction: A technical overview," *IEEE Signal Process. Mag.*, vol. 20, no. 3, pp. 21–36, May 2003, doi: 10.1109/MSP.2003.1203207.

[2] Y. Jiang, Y. Lu, L. Dong, and W. Xu, "Multi-frame image super-resolution algorithm based on small amount of data," in *Proc. IEEE 5th Int. Conf. Image, Vis. Comput. (ICIVC)*, Jul. 2020, pp. 118–122, doi: 10.1109/ICIVC50857.2020.9177476.

[3] L. Yue, H. Shen, J. Li, Q. Yuanc, H. Zhang, and L. Zhang, "Image super-resolution: The techniques, applications, and future," *Signal Process.*, vol. 128, pp. 389–408, Nov. 2016, doi: 10.1016/j.sigpro.2016.05.002.

[4] Y. Chen, V. Phonevilay, J. Tao, X. Chen, R. Xia, Q. Zhang, Y. Kai, X. Jie, and J. Xie, "The face image super-resolution algorithm based on combined representation learning," *Multimedia Tools Appl.*, vol. 80, no. 20, pp. 30839–30861, 2020.

[5] Y. Fu, T. Zhang, Y. Zheng, D. Zhang, and H. Huang, "Hyperspectral image super-resolution with optimized RGB guidance," in *Proc. IEEE/CVF Conf. Comput. Vis. Pattern Recognit. (CVPR)*, Jun. 2019, pp. 11661–11670.

[6] Y. Chen, L. Liu, V. Phonevilay, J. Tao, X. Chen, R. Xia, Q. Zhang, Y. Kai, X. Jie, and J. Xie, "Image super-resolution reconstruction based on feature map attention mechanism," *Appl. Intell.*, vol. 51, no. 7, pp. 4367–4380, 2021.

[7] B. Wronski, I. Garcia-Dorado, M. Ernst, D. Kelly, M. Krainin, C.-K. Liang, M. Levoy, and P. Milanfar, "Handheld multi-frame super-resolution," *ACM Trans. Graph.*, vol. 38, no. 4, pp. 1–18, Jul. 2019, doi: 10.1145/3306346.3323024.

[8] T. S. Huang and R. Y. Tsay, "Multiple frame image restoration and registration," in *Proc. Adv. Comput. Vis. Image Process.*, vol. 1, 1984, pp. 317–339.

[9] S. P. Kim, N. K. Bose, and H. M. Valenzuela, "Recursive reconstruction of high resolution image from noisy undersampled multiframes," *IEEE Trans. Acoust., Speech, Signal Process.*, vol. 38, no. 6, pp. 1013–1027, Jun. 1990, doi: 10.1109/29.56062.

[10] N. K. Bose, H. C. Kim, and H. M. Valenzuela, "Recursive implementation of total least squares algorithm for image reconstruction from noisy, under-sampled multiframes," in *Proc. IEEE Int. Conf. Acoust., Speech, Signal Process.*, vol. 5, Minneapolis, MN, USA, Apr. 1993, pp. 269–272, doi: 10.1109/ICASSP.1993.319799.

[11] S. Rhee and M. Gi Kang, "DCT-based regularized algorithm for high-resolution image reconstruction," in *Proc. Int. Conf. Image Process.*, Oct. 1999, pp. 184–187, doi: 10.1109/ICIP.1999.817096.

[12] H. Ur and D. Gross, "Improved resolution from subpixel shifted pictures," *CVGIP, Graph. Models Image Process.*, vol. 54, no. 2, pp. 181–186, Mar. 1992.

[13] S. Shivagunde and M. Biswas, "Single image super-resolution based on modified interpolation method using MLP and DWT," in *Proc. 3rd Int. Conf. Trends Electron. Informat. (ICOEI)*, Apr. 2019, pp. 212–219, doi: 10.1109/ICOEI.2019.8862571.

[14] R. Seema and K. Bailey, "Multi-frame image super-resolution by interpolation and iterative backward projection," in *Proc. 2nd Int. Conf. Signal Process. Commun. (ICSPC)*, Mar. 2019, pp. 36–40, doi: 10.1109/ICSPC46172.2019.8976500.

[15] M. Irani and S. Peleg, "Improving resolution by image registration," *CVGIP, Graph. Models Image Process.*, vol. 53, no. 3, pp. 231–239, May 1991.

[16] H. Song, X. He, W. Chen, and Y. Sun, "An improved iterative back-projection algorithm for video super-resolution reconstruction," in *Proc. Symp. Photon. Optoelectron.*, Jun. 2010, pp. 1–4, doi: 10.1109/SOPO.2010.5504209.

[17] J.-S. Yoo and J.-O. Kim, "Noise-robust iterative back-projection," *IEEE Trans. Image Process.*, vol. 29, pp. 1219–1232, 2020, doi: 10.1109/TIP.2019.2940414.

[18] A. J. Patti and Y. Altunbasak, "Artifact reduction for set theoretic super resolution image reconstruction with edge adaptive constraints and higher-order interpolants," *IEEE Trans. Image Process.*, vol. 10, no. 1, pp. 179–186, Jan. 2001, doi: 10.1109/83.892456.

[19] C. Fan, C. Wu, G. Li, and J. Ma, "Projections onto convex sets super-resolution reconstruction based on point spread function estimation of low-resolution remote sensing images," *Sensors*, vol. 17, no. 2, p. 362, Feb. 2017, doi: 10.3390/s17020362.

[20] Z. Ma and G. Ren, "Projection onto the convex sets model based on non-downsampling contourlet transform and high-frequency iteration," *Electron. Lett.*, vol. 56, no. 20, pp. 1054–1056, Sep. 2020, doi: 10.1049/el.2020.0364.

[21] S. A. Shirazi and M. Yazdi, "A new approach in super resolution based on an adaptive regularization parameter," in *Proc. 3rd Int. Symp. Commun., Control Signal Process.*, Mar. 2008, pp. 572–577, doi: 10.1109/ISCCSP.2008.4537290.

[22] K. Tan, W. Li, J. Pei, Y. Huang, and J. Yang, "An I/Q-channel modeling maximum likelihood super-resolution imaging method for forward-looking scanning radar," *IEEE Geosci. Remote Sens. Lett.*, vol. 15, no. 6, pp. 863–867, Jun. 2018, doi: 10.1109/LGRS.2018.2811043.

[23] H. Shen, L. Zhang, B. Huang, and P. Li, "A MAP approach for joint motion estimation, segmentation, and super resolution," *IEEE Trans. Image Process.*, vol. 16, no. 2, pp. 479–490, Feb. 2007, doi: 10.1109/TIP.2006.888334.

[24] S. P. Belekos, N. P. Galatsanos, and A. K. Katsaggelos, "Maximum a posteriori video super-resolution using a new multichannel image prior," *IEEE Trans. Image Process.*, vol. 19, no. 6, pp. 1451–1464, Jun. 2010, doi: 10.1109/TIP.2010.2042115.

[25] H. Irmak, G. B. Akar, and S. E. Yuksel, "A MAP-based approach for hyperspectral imagery super-resolution," *IEEE Trans. Image Process.*, vol. 27, no. 6, pp. 2942–2951, Jun. 2018, doi: 10.1109/TIP.2018.2814210.

[26] W. Zheng, F. Deng, S. Mo, X. Jin, Y. Qu, J. Zhou, R. Zou, J. Shuai, Z. Xie, S. Long, and C. Zheng, "Image super-resolution reconstruction algorithm based on Bayesian theory," in *Proc. 13th IEEE Conf. Ind. Electron. Appl. (ICIEA)*, May 2018, pp. 1934–1938, doi: 10.1109/ICIEA.2018.8398025.

[27] T. P. Do Nascimento and E. O. T. Salles, "Multi-frame super-resolution combining demons registration and Bayesian regularized reconstruction," *IEEE Signal Process. Lett.*, vol. 27, pp. 2009–2013, Oct. 2020, doi: 10.1109/LSP.2020.3033422.

[28] M. Elad and A. Feuer, "Superresolution restoration of an image sequence: Adaptive filtering approach," *IEEE Trans. Image Process.*, vol. 8, no. 3, pp. 387–395, Mar. 1999, doi: 10.1109/83.748893.

[29] J. Anver and A. Parambil, "Single-image super-resolution using online kernel adaptive filters," *IET Image Process.*, vol. 13, no. 11, pp. 1846–1852, Sep. 2019, doi: 10.1049/IET-IPR.2018.5319.

[30] S. Farsiu, M. D. Robinson, M. Elad, and P. Milanfar, "Fast and robust multiframe super resolution," *IEEE Trans. Image Process.*, vol. 13, no. 10, pp. 1327–1344, Oct. 2004, doi: 10.1109/TIP.2004.834669.

[31] V. Patanavijit and S. Jitapunkul, "A robust iterative multiframe super-resolution reconstruction using a Bayesian approach with Lorentzian norm," in *Proc. 10th IEEE Singap. Int. Conf. Commun. Syst.*, Oct. 2006, pp. 1–5, doi: 10.1109/ICCS.2006.301414.

[32] R. C. Hardie, K. J. Barnard, and E. E. Armstrong, "Joint MAP registration and high-resolution image estimation using a sequence of undersampled images," *IEEE Trans. Image Process.*, vol. 6, no. 12, pp. 1621–1633, Dec. 1997, doi: 10.1109/83.650116.

[33] H. Rezayi and S. A. Seyedin, "Huber Markov random field for joint super resolution," in *Proc. 10th Iranian Conf. Mach. Vis. Image Process. (MVIP)*, Nov. 2017, pp. 93–98, doi: 10.1109/IranianMVIP.2017.8342375.

[34] M. K. Ng, H. Shen, E. Y. Lam, and L. Zhang, "A total variation regularization based super-resolution reconstruction algorithm for digital video," *EURASIP J. Adv. Signal Process.*, vol. 2007, no. 1, pp. 1–16, Dec. 2007, doi: 10.1155/2007/74585.

[35] Q. Zhang, Y. Zhang, Y. Huang, Y. Zhang, W. Li, and J. Yang, "Total variation superresolution method for radar forward-looking imaging," in *Proc. 6th Asia–Pacific Conf. Synth. Aperture Radar (APSAR)*, Xiamen, China, 2019, pp. 1–4, doi: 10.1109/APSAR46974.2019.9048388.

[36] S. Terai and T. Goto, "Noise removal super-resolution for camera images utilizing total variation regularization method," in *Proc. IEEE 2nd Global Conf. Life Sci. Technol. (LifeTech)*, Mar. 2020, pp. 183–184, doi: 10.1109/LifeTech48969.2020.1570619113.

[37] A. R. V and S. N. George, "Multi-frame image super resolution using spatially weighted total variation regularisations," *IET Image Process.*, vol. 14, no. 10, pp. 2187–2194, Aug. 2020, doi: 10.1049/iet-ipr.2019.0901.

[38] Y. Chen, H. Zhang, L. Liu, J. Tao, Q. Zhang, K. Yang, R. Xia, and J. Xie, "Research on image inpainting algorithm of improved total variation minimization method," *J. Ambient Intell. Humanized Comput.*, pp. 1–10, Jan. 2021, doi: 10.1007/S12652-020-02778-2.

[39] G. Chantas, N. Galatsanos, R. Molina, and A. Katsaggelos, "Variational Bayesian inference image restoration using a product of total variation-like image priors," in *Proc. 2nd Int. Workshop Cognit. Inf. Process.*, Jun. 2010, pp. 227–231, doi: 10.1109/CIP.2010.5604259.

[40] G. Chantas, N. Galatsanos, A. Likas, and M. Saunders, "Variational Bayesian image restoration based on a product of *t*-distributions image prior," *IEEE Trans. Image Process.*, vol. 17, no. 10, pp. 1795–1805, Oct. 2008, doi: 10.1109/TIP.2008.2002828.

[41] S. Villena, M. Vega, S. D. Babacan, R. Molina, and A. K. Katsaggelos, "Bayesian combination of sparse and non-sparse priors in image super resolution," *Digit. Signal Process.*, vol. 23, no. 2, pp. 530–541, 2013, doi: 10.1016/j.dsp.2012.10.002.

[42] S. Villena, M. Vega, R. Molina, and A. K. Katsaggelos, "A non-stationary image prior combination in super-resolution," *Digit. Signal Process.*, vol. 32, pp. 1–10, Sep. 2014, doi: 10.1016/J.DSP.2014.05.017.

[43] L. Min, P. Yang, L. Dong, W. Liu, S. Wang, B. Xu, and Y. Liu, "A l1 norm based image prior combination in multiframe superresolution," *Math. Problems Eng.*, vol. 2017, pp. 1–15, Nov. 2017, doi: 10.1155/2017/2694638.

[44] K. He, J. Sun, and X. Tang, "Single image haze removal using dark channel prior," *IEEE Trans. Pattern Anal. Mach. Intell.*, vol. 33, no. 12, pp. 2341–2353, Dec. 2011, doi: 10.1109/TPAMI.2010.168.

[45] J. Pan, D. Sun, H. Pfister, and M.-H. Yang, "Deblurring images via dark channel prior," *IEEE Trans. Pattern Anal. Mach. Intell.*, vol. 40, no. 10, pp. 2315–2328, Oct. 2018, doi: 10.1109/TPAMI.2017.2753804.

[46] Y. Yan, W. Ren, Y. Guo, R. Wang, and X. Cao, "Image deblurring via extreme channels prior," in *Proc. IEEE Conf. Comput. Vis. Pattern Recognit. (CVPR)*, Jul. 2017, pp. 6978–6986, doi: 10.1109/CVPR.2017.738.

[47] S. Cao, W. Tan, K. Xing, H. He, and J. Jiang, "Dark channel inspired deblurring method for remote sensing image," *J. Appl. Remote Sens.*, vol. 12, no. 1, p. 1, Feb. 2018.

[48] D. Strong and T. Chan, "Edge-preserving and scale-dependent properties of total variation regularization," *Inverse Probl.*, vol. 19, no. 6, pp. 165–187, Dec. 2003, doi: 10.1088/0266-5611/19/6/059.

[49] J. Yang, W. Yin, Y. Zhang, and Y. Wang, "A fast algorithm for edge-preserving variational multichannel image restoration," *SIAM J. Imag. Sci.*, vol. 2, no. 2, pp. 569–592, 2009, doi: 10.1137/080730421.

[50] J. M. Bioucas-Dias, M. A. T. Figueiredo, and J. P. Oliveira, "Total variation-based image deconvolution: A majorization-minimization approach," in *Proc. IEEE Int. Conf. Acoust., Speech Signal Process.*, Toulouse, France, vol. 2, Jul. 2006, pp. 861–864.

[51] L. Xu, C. Lu, Y. Xu, and J. Jia, "Image smoothing via L0 gradient minimization," in *Proc. SIGGRAPH Asia Conf.*, 2011, pp. 1–12.

[52] L. C. Pickup, D. P. Capel, S. J. Roberts, and A. Zisserman, "Bayesian methods for image super-resolution," *Comput. J.*, vol. 52, no. 1, pp. 101–113, Feb. 2008.

[53] Y. He, K. H. Yap, L. Chen, and L. P. Chau, "A nonlinear least square technique for simultaneous image registration and super-resolution," *IEEE Trans. Image Process.*, vol. 16, no. 11, pp. 2830–2841, Nov. 2007, doi: 10.1109/TIP.2007.908074.

[54] C. Liu and D. Sun, "On Bayesian adaptive video super resolution," *IEEE Trans. Pattern Anal. Mach. Intell.*, vol. 36, no. 2, pp. 346–360, Feb. 2014, doi: 10.1109/TPAMI.2013.127.

SHEN SHI received the B.S. degree from Hainan University, Hainan, China, in 2011. He is currently pursuing the Ph.D. degree with Shanghai Institute of Microsystem and Information Technology, Chinese Academy of Sciences, and with ShanghaiTech University, Shanghai, China. His research interests include remote sensing image processing and super resolution.
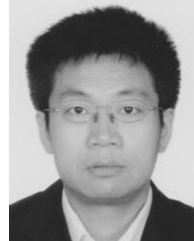
ZENGSHAN YIN received the Ph.D. degree from Zhejiang University, Zhejiang, China. He is currently a Professor with the Innovation Academy for Microsatellites, Chinese Academy of Sciences, Shanghai, China. His current research interests include microsatellite system design and remote sensing image processing and application technology.

ZHIMING MEI is currently pursuing the Ph.D. degree in remote sensing with the Innovation Academy for Microsatellites, Chinese Academy of Sciences, China, and the University of Chinese Academy of Sciences, Beijing, China.

His research interests include deep learning, computer vision, high-dimensional data process, and their applications in the context of hyperspectral image.

LONG WANG received the Ph.D. degree in communication engineering from the University of Chinese Academy of Sciences, Beijing, China, in 2019. He is currently a Researcher with the Innovation Academy for Microsatellites, Chinese Academy of Sciences, Shanghai, China. His research interests include satellite networks, space optical communication, and space-based information networks.

● ● ●